

## **Effect of Microcracks on the Corrosion Behaviour of Fe-based amorphous coatings in Chloride Solutions**

*Jin Jiao<sup>1</sup>, Qiang Luo<sup>1</sup>, Xianshun Wei<sup>1</sup>, Shoujiang Qu<sup>1</sup>, Yong Wang<sup>2</sup>, Jun Shen<sup>1,\*</sup>*

<sup>1</sup> School of Materials Science and Engineering, Tongji University, 4800 Caoan Road, Shanghai 201804, China

<sup>2</sup> School of Mechanical Science and Engineering, Northeast Petroleum University, 199 Fazhan Road, Daqing 163318, China

\*E-mail: [junshen@tongji.edu.cn](mailto:junshen@tongji.edu.cn)

*Received:* 13 February 2018 / *Accepted:* 8 April 2018 / *Published:* 10 May 2018

---

In this paper, the influence of microcracks on the corrosion behaviour of Fe-based amorphous coating on 304 stainless steel in 3.5 wt.% NaCl solution was investigated. Results show that microcracks deteriorate the corrosion resistance. The corrosive solution can penetrate into the microcracks, resulting in the direct corrosion of the substrate. Furthermore, the pitting potential of the substrate at the coating–substrate interface is apparently lower than that of the uncoated substrate, which is ascribed to the crevice corrosion caused by through-microcracks. As a result, the coated substrate is more prone to corrosion than the uncoated substrate. The microcracks can be effectively sealed by aluminium phosphate sealant, which improves the protectiveness of amorphous coating.

---

**Keywords:** amorphous coating; sealing treatment; microcrack; corrosion behaviour

### **1. INTRODUCTION**

Fe-based amorphous alloy possesses outstanding mechanical properties and corrosion resistance, while its cost is not high [1–3]. Although Fe-based amorphous alloy has been widely investigated, it is hardly applied in industry as structure material due to its extreme brittleness at room temperature and limited glass forming ability [4–6]. Thermal spray technology can be used to prepare Fe-based amorphous coatings, which effectively expand its application range [7–9]. However, structural defects, including porosity and oxides, inevitably exist in Fe-based amorphous coating, which form during thermal spray process.

The corrosion behaviour of Fe-based amorphous coating is significantly affected by structural defects [10–15]. Specifically, the inferior corrosion resistance of Fe-based amorphous coating to that

of the equivalent ribbon and bulk material is attributed to structural defects [16–19]. Therefore, the role of structural defects in the corrosion behaviour of Fe-based amorphous coating has been studied in recent years [20–24]. Zhang et al. [21] found that in Fe-based amorphous coating, the oxygen is concentrated at the interface of splats in the form of nano-oxides and the oxidised boundary is preferentially corroded. Zhang et al. [22] further found that the formation of oxides,  $(\text{Cr, Fe})_2\text{O}_3$  and  $\text{FeCr}_2\text{O}_4$ , at the intersplat region leads to the emergence of Cr-depleted zone, where pitting initiates. Zhang et al. [23] directly observed the preferential corrosion of the substrate beneath the Fe-based amorphous coating caused by through-porosity via three-dimensional X-ray tomography technique. Zhang et al. [24] found that porosity deteriorates the long-term corrosion resistance of Fe-based amorphous coating due to Cr-depleted zones around porosity that trigger corrosion.

Microcracks also exist in Fe-based amorphous coating and their effect on corrosion behaviour is usually ignored. However, we found that microcracks play a significant role in corrosion process. In this work, high-velocity air fuel (HVOF) spray process was used to prepare the Fe-based amorphous coatings and the effect of microcracks on the corrosion behaviour was systematically investigated. To clarify the corrosion mechanism, microcrack-free amorphous coating was prepared by sealing treatment. We found that the through-microcracks do not only lead to the direct corrosion of the substrate by the penetration of corrosive solution, but also result in the decreased pitting potential of the coated substrate.

## 2. EXPERIMENTAL

The diameter of amorphous powders used for spray ranged from 25–38  $\mu\text{m}$  and the nominal composition is  $\text{Fe}_{49.7}\text{Cr}_{18}\text{Mo}_{7.4}\text{Mn}_{1.9}\text{W}_{1.6}\text{C}_{3.8}\text{B}_{15.2}\text{Si}_{2.4}$  (at.%). The size of the substrate is 180 mm  $\times$  90 mm  $\times$  8 mm. All substrates were smoothed by a grinding machine, degreased by acetone, and then grit-blasted before thermal spraying. The HVOF spray system used for coating preparation and the detailed spraying parameters were described in a previous work [25].

Aluminium phosphate sealant was selected to seal the as-sprayed coatings and the detailed sealing treatment procedure was described in our previous work [25]. Excess sealant on sealed coating surface was removed by abrasive paper to expose the true coating surface for test. The microstructure of the feedstock powders and coatings was characterized by X-ray diffraction (XRD, D/MAX 2550VB3+) and scanning electron microscopy (SEM, TESCAN and FEI Quanta FEG 250) coupled with energy dispersive spectroscopy (EDS). The porosity of the coating was measured using SEM secondary electron micrograph analysis with the Image Pro-Plus version 6.0 software.

Electrochemical measurements of the unsealed and sealed coatings were performed in 3.5 wt.% NaCl solution at room temperature by using an electrochemical workstation (Gamry Reference 600). All electrochemical tests were conducted in a typical three-electrode cell, including a saturated calomel electrode (SCE) and a large platinum mesh, which function as the reference electrode and the counter electrode respectively. The test surfaces of samples were polished to mirror finish first, then cleaned in ethanol and distilled water ultrasonically in sequence, and finally dried in warm air prior to the electrochemical test. The samples were immersed in solution for half an hour to attain a steady open-

circuit potential (OCP) before starting all electrochemical measurements. Potentiodynamic polarization test was conducted from  $-0.5$  V (vs. OCP) to  $1.2$  V (vs.  $V_{SCE}$ ) at a fixed sweep rate of  $0.5$  mV/s. Electrochemical impedance spectroscopy (EIS) measurements were performed with sinusoidal amplitude of  $10$  mV at OCP. The frequency range is between  $0.01$  and  $10000$  Hz. The fitting of EIS results based on the equivalent circuits was used Zview software.

### 3. RESULTS AND DISCUSSION

#### 3.1. Characterisation of powders and coatings

The powder morphology shown in Fig. 1a exhibits the nearly spherical shape and smooth surface of powders. The XRD patterns of the as-sprayed coating and powders displayed in Fig. 1b are similar. The appearance of some crystalline diffraction peaks and a broad diffraction hump indicates the coexistence of the crystalline and amorphous phases. Compared to the coating, the broad diffraction hump of powders is a little weaker, implying the lower content of amorphous phase. The similar phenomena have been reported in previous studies that the amorphous phase content of thermal spray coating is higher than that of the feedstock powders [8,11,19,26–29]. The reason is considered to be the quenching of completely or partially molten particles during the impact onto the substrate surface, which leads to the formation of amorphous phase [11,19,28,29].

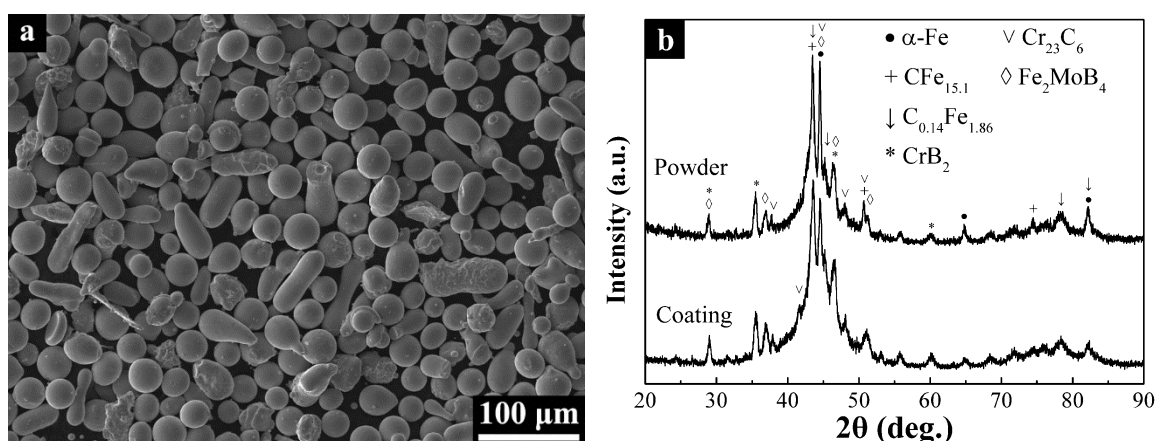


**Figure 1.** (a) SEM image of feedstock powders; (b) XRD patterns of Fe-based amorphous powders and coating.

The morphologies of the surface and cross-section of the as-sprayed coating are shown in Fig. 2. The vertical microcracks are visible in addition to pores in the coating. The thickness and porosity of coating are  $380 \mu\text{m}$  and  $1.6\%$ , respectively. Fig. 3a shows the cross-sectional morphology of the sealed coating. The selected area in Fig. 3a is studied with EDS and the elemental mapping result of phosphorus is illustrated in Fig. 3b. It is found that the aluminium phosphate sealant penetrates into the microcrack at a depth of approximately  $85 \mu\text{m}$  according to the distribution of phosphorus element. The magnified morphology of the topside of the microcrack in Fig. 3a is displayed in Fig. 3c. Fig. 3d

presents the elemental mapping result of phosphorus of the selected area in Fig. 3c. As shown in Figs. 3b and d, the distribution of phosphorus element is almost only limited in the microcrack, which suggests that only the microcracks and not the pores are penetrated by the aluminium phosphate sealant.

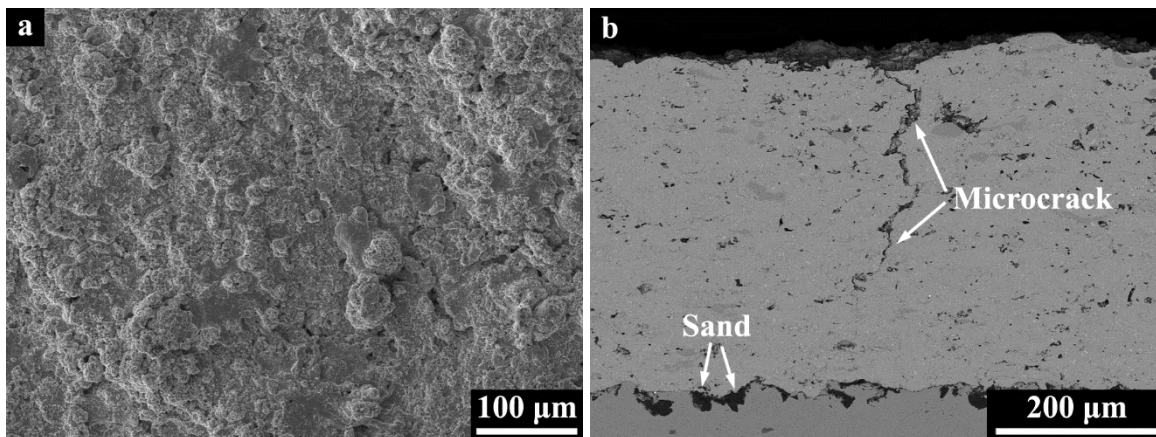


Figure 2. SEM micrographs of the (a) surface and (b) cross-section of the as-deposited coating.

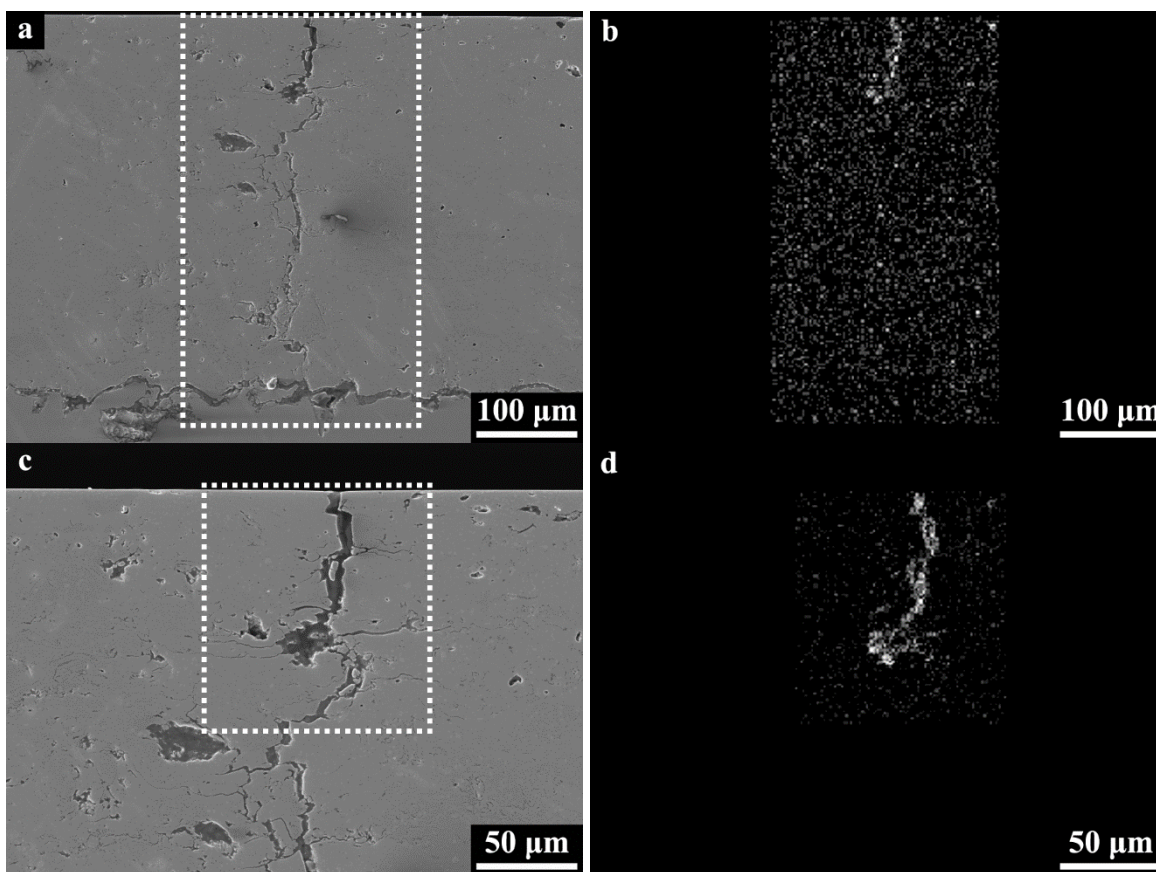
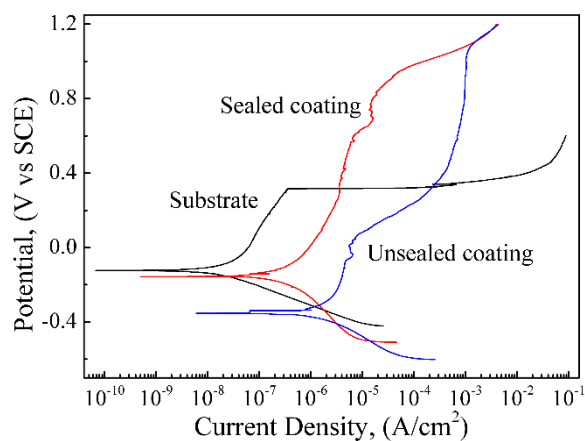


Figure 3. (a) SEM micrograph of cross-section of the sealed coating; (c) The enlarged image of the topside of the microcrack from (a); (b) and (d) are the phosphorus maps for the selected area of (a) and (c), respectively.

This result may be attributed to the relatively low porosity of the coating, which virtually exhibits closed porosity and is impossible to seal. Previous works have also shown that the aluminium phosphate sealant can penetrate into thermal spray coating and seal internal structural defects, such as pores and microcracks [14,15,25,30].

### 3.2. Potentiodynamic polarization

The potentiodynamic polarization curves of coatings and substrate are shown in Fig. 4. The corresponding corrosion parameters, including corrosion potential ( $E_{\text{corr}}$ ), corrosion current density ( $i_{\text{corr}}$ ), pitting potential ( $E_{\text{pit}}$ ) and passive current density ( $i_{\text{pass}}$ ), are summarized in Table 1. It is noted that the pitting potential of the substrate is much lower than that of the sealed coating. Compared with the unsealed coating, the sealed coating has higher corrosion potential and lower passivation current density and corrosion current density, which is consistent with the previous work [14,15,25]. This result illustrates the effectiveness of aluminium phosphate sealing treatment in improving the corrosion resistance of the Fe-based amorphous coating. It is worth noting that the unsealed coating exhibits peculiar anodic polarization behaviour.



**Figure 4.** Potentiodynamic polarization curves of unsealed and sealed coatings in comparison with the substrate in 3.5 wt.% NaCl solution.

The passive current density of the unsealed coating increases significantly as the potential exceeds 0 V<sub>SCE</sub>. A similar result has been reported by Zhang in the Fe-based amorphous coating with the same composition [23]. They found that the anodic current density increases distinctly as the potential exceeds 0.3 V<sub>SCE</sub>, which is due to the pitting corrosion of the substrate (304 stainless steel). However, in the present paper, the anodic current density increases sharply at a lower potential, which is related to the crevice corrosion of the substrate. The detailed discussion is shown in Section 3.5. The surface morphologies of the coatings before and after potentiodynamic polarization are displayed in Fig. 5. Only a few corrosion products are distributed homogeneously on the sealed coating surface after potentiodynamic polarization, whereas a considerable amount of corrosion products pile up at the

microcrack on the unsealed coating surface. This result reveals that the corrosive solution can penetrate into the microcrack and reach the substrate. Therefore, the substrate beneath the microcrack in unsealed coating has been corroded seriously and much corrosion products formed. However, the microcracks have been blocked after sealing treatment, which prevents the penetration of corrosive solution. Thus only a small amount of corrosion products is present on the sealed coating surface after potentiodynamic polarization due to the corrosion of the amorphous coating.

**Table 1.** The corrosion parameters of substrate and coatings obtained from potentiodynamic polarization tests.

Samples	$E_{corr}$ (V <sub>SCE</sub> )	$i_{corr}$ (A/cm <sup>2</sup> )	$E_{pit}$ (V <sub>SCE</sub> )	$i_{pass}$ (A/cm <sup>2</sup> )
Substrate	-0.130	$2.73 \times 10^{-8}$	0.314	$1.30 \times 10^{-7}$
Sealed coating	-0.156	$7.68 \times 10^{-7}$	0.833	$5.04 \times 10^{-6}$
Unsealed coating	-0.353	$1.40 \times 10^{-6}$	1.039	$5.78 \times 10^{-4}$

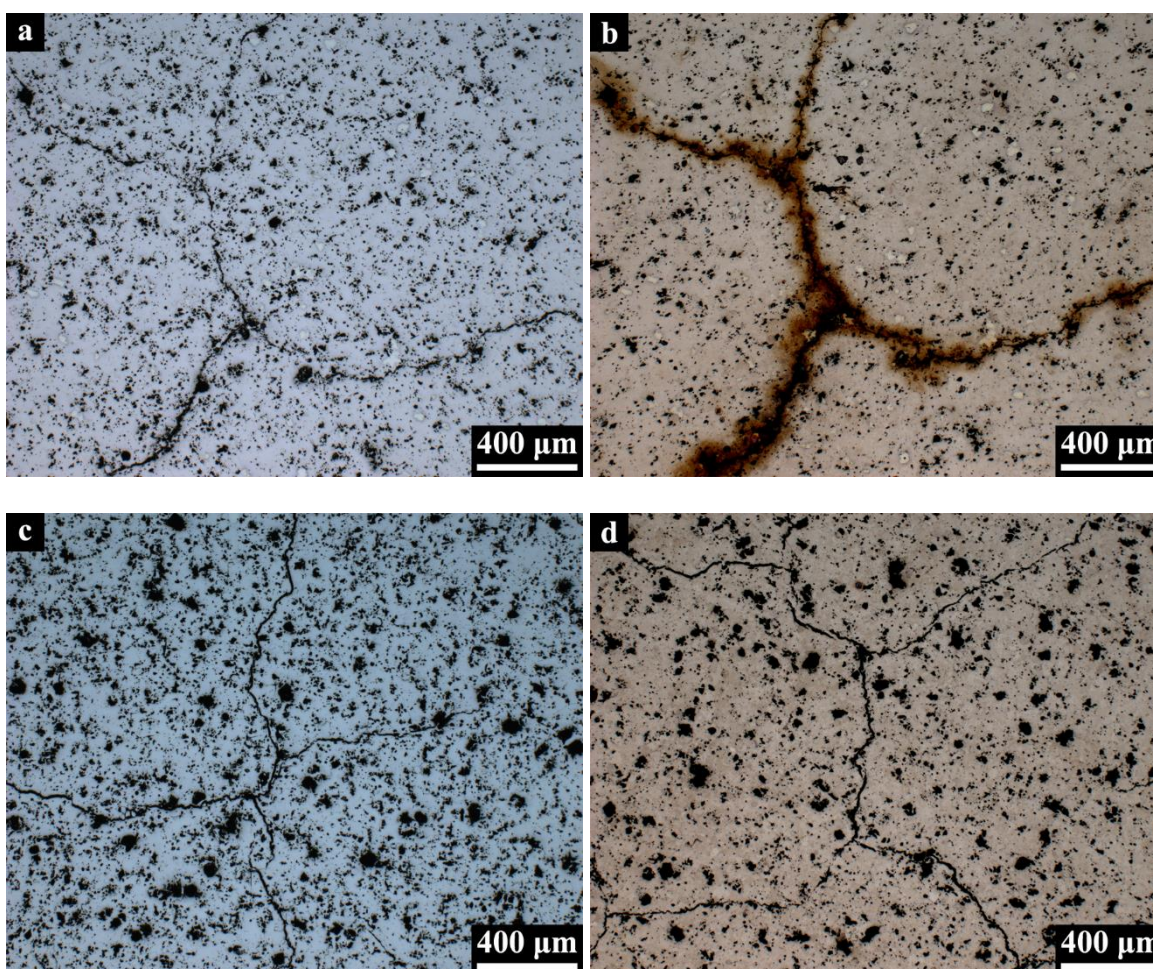
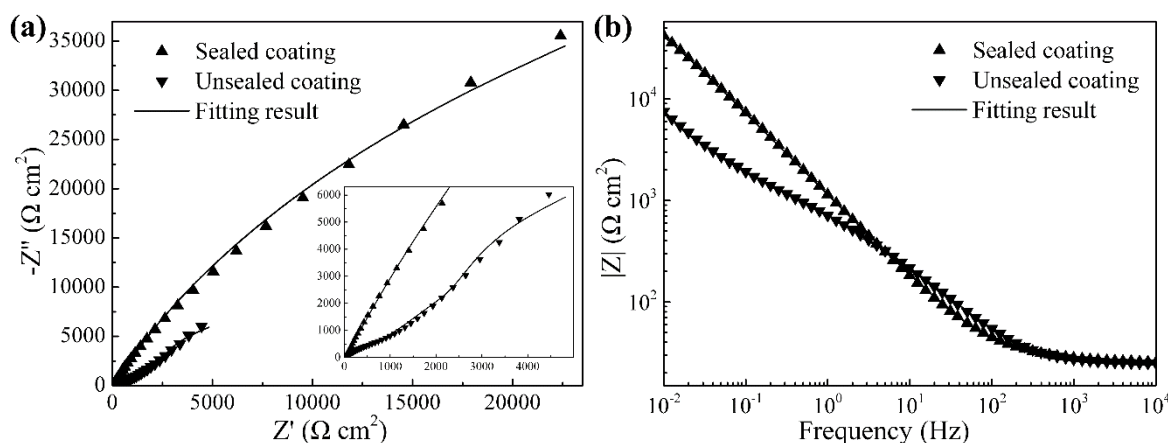


**Figure 5.** Optical images of the surfaces of (a, b) unsealed and (c, d) sealed coatings (a, c) before and (b, d) after potentiodynamic polarization test in 3.5 wt.% NaCl solution.

3.3. EIS

The EIS spectra of the coatings are presented in Fig. 6. The Nyquist plot of unsealed coating shows a straight line with a slope of approximately 45° at low frequency, implying the generation of Warburg impedance when the charge transfer is affected by a semi-infinite length diffusion process [31,32]. The EIS data is simulated by two equivalent electrical circuits respectively as shown in Fig. 7. A constant phase element (CPE) is usually used instead of pure capacitance in real electrochemical processes [33]. The equivalent circuit in Fig. 7a consists of the solution resistance ( $R_s$ ), the capacitance of the coating (CPE-c) and the resistance of the coating ( $R_c$ ). In addition to the  $R_s$  and CPE-c, the equivalent circuit in Fig. 7b comprises  $R_p$ ,  $Z_w$ , CPE-d and  $R_t$ , which denote the resistance of the through-microcracks, the Warburg impedance, the capacitance of the double layer and the reaction resistance at the substrate-coating interface, respectively. The dielectric properties of the coating are represented by the parallel elements of CPE-c and  $R_p$ , whereas the charge transfer process at the substrate-coating interface beneath the through-microcrack is described by the other elements of CPE-d and  $R_t$  in parallel. On the basis of the equivalent electrical circuits, the calculated EIS curves are also presented in Fig. 6 as the solid lines. The fitting parameters of equivalent electrical circuits are summarised in Table 2.

The sealed coating shows one time constant, whereas the unsealed coating exhibits two time constants as shown in Fig. 6, suggesting the corrosion of the substrate beneath the through-microcracks. The emergence of the Warburg impedance in Fig. 6 is also related to the through-microcracks. As shown in Fig. 6b, the impedance magnitude of unsealed coating is lower than that of sealed coating, especially in the low-frequency range, implying the weak protectiveness of the unsealed coating [34]. This result is confirmed by the fitting results of equivalent electrical circuits. The values of  $R_p$  and  $R_t$  for the unsealed coating are pretty low, implying the permeation of corrosive solution. By comparison, the  $R_c$  value of the sealed coating is very high, indicating the effectiveness of the sealing treatment. These results further demonstrate that the sealing treatment significantly increases the protectiveness of amorphous coating in 3.5 wt.% NaCl solution, which agrees well with the previous results of potentiodynamic polarization test.



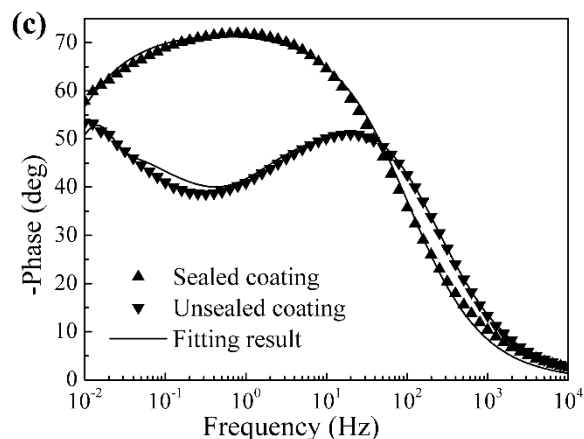


**Figure 6.** EIS plots of sealed and unsealed coatings in 3.5 wt.% NaCl solution. (a) Nyquist plots, (b) Bode impedance magnitude plots, (c) Bode phase angle plots.

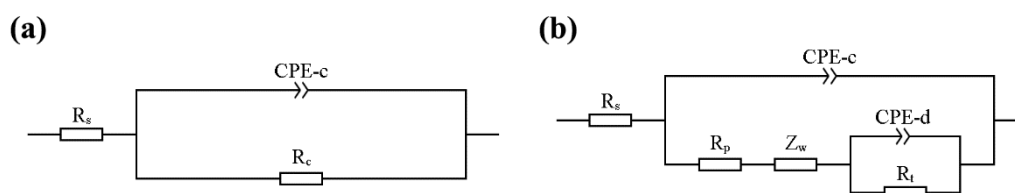


**Figure 7.** General model of the equivalent circuits used to fit the EIS data of the (a) sealed coating and (b) unsealed coating.

**Table 2.** The fitting parameters of the equivalent electrical circuits obtained from the EIS spectra for unsealed and sealed coatings.

Samples	$R_s$ ( $\Omega \text{ cm}^2$ )	CPE-c ( $\mu\text{F}/\text{cm}^2$ )	$\eta_{\text{CPE-c}}$	$R_p/R_c$ ( $\Omega \text{ cm}^2$ )	CPE-d ( $\mu\text{F}/\text{cm}^2$ )	$\eta_{\text{CPE-d}}$	$R_t$ ( $\Omega \text{ cm}^2$ )
Unsealed coating	24.28	151.45	0.79	519.6	324.45	0.87	265.9
					$Z_w$		
					$R$ ( $\Omega \text{ cm}^2$ )	$\tau$ (s)	$p$
Sealed coating	26.46	199.03	0.81	143230	13149	49.43	0.59

### 3.4. Potentiostatic polarization

To further investigate the corrosion mechanism of unsealed coating, potentiostatic polarization measurement was conducted in 3.5 wt.% NaCl solution at 0.2  $V_{\text{SCE}}$  for 10000 s. The resulting current density–time curve is shown in Fig. 8. The current density increases rapidly until about 2000 seconds after the oscillation in the first 70 seconds, and thereafter fluctuates within a small range. The cross-section and surface morphologies of the unsealed coating after potentiostatic polarization test are

displayed in Fig. 9. As shown in Fig. 9a there is a microcrack through the cross-section of the coating. The substrate at the coating–substrate interface has been corroded seriously while the amorphous coating seems unchanged, which generates a gap between the coating and substrate, especially near the microcrack.

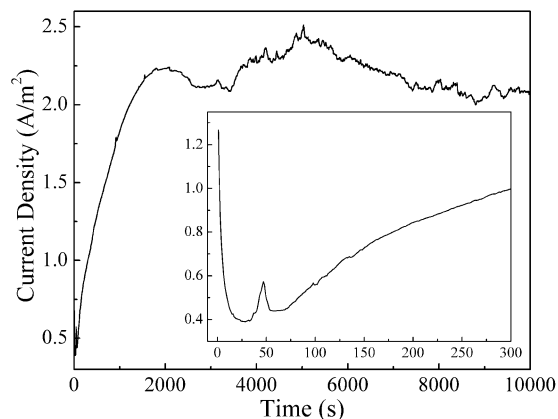


**Figure 8.** Current density–time curve of potentiostatic polarization of unsealed coating at 0.2 V<sub>SCE</sub> in 3.5 wt.% NaCl solution.

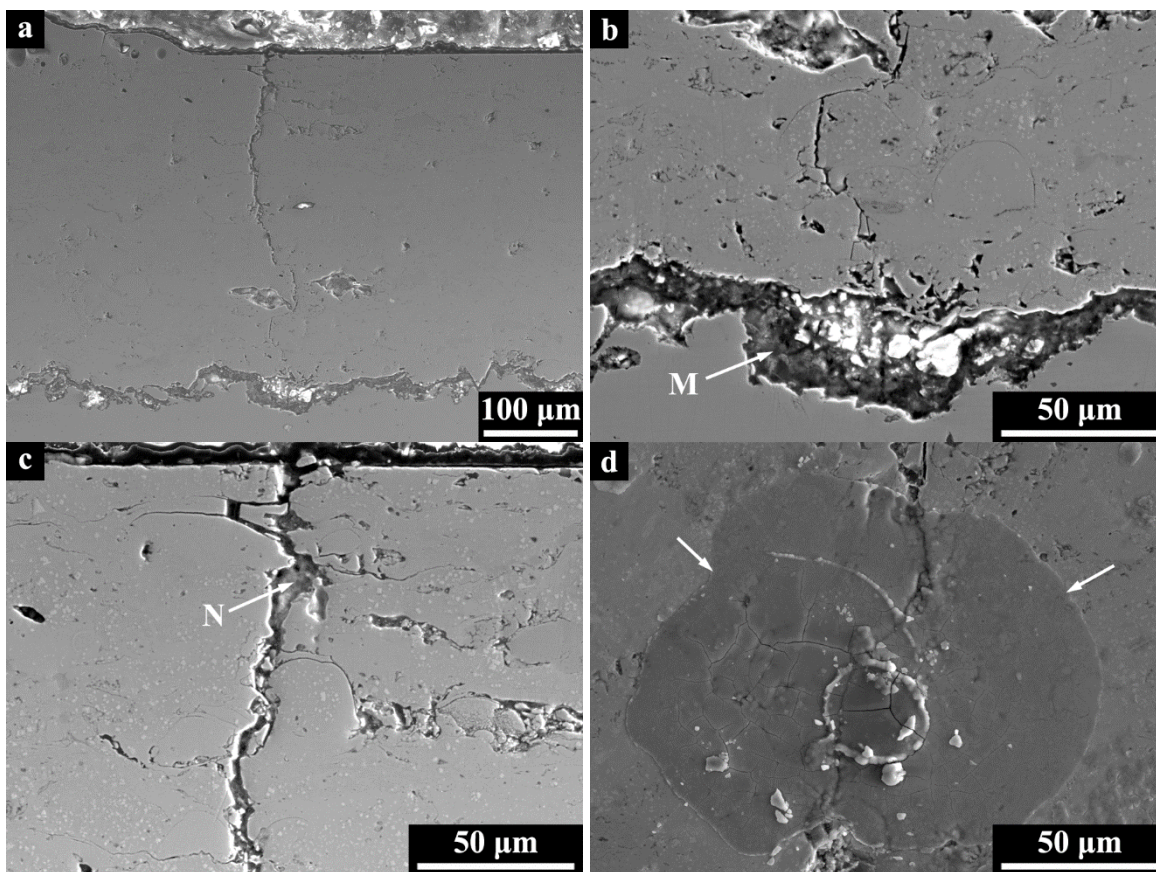


**Figure 9.** (a–c) Cross-section and (d) surface morphologies of unsealed coating after potentiostatic polarization test in 3.5 wt.% NaCl solution; (b) and (c) are the high magnifications of the bottom and topside of the microcrack in (a), respectively.

The high magnifications of the bottom and the topside of the microcrack are presented in Figs. 9b and c respectively, from which it is noted that the microcrack and the gap between the coating and substrate are almost completely filled. Further EDS analysis results of points M and N (Table 3) exhibit similar composition of both points with high content of oxygen and iron, revealing that it is corrosion products that fill in the gap and the microcrack.

**Table 3.** Chemical composition (at.%) of points M and N in Figure 9.

Location	C	O	Si	Cl	Cr	Fe	Mo
Point M	7.17	43.66	1.14	1.32	4.33	42.38	–
Point N	8.58	53.1	1.54	–	3.22	32.92	0.64

### 3.5. Corrosion mechanism

Although the potentiostatic polarization test was performed at a lower potential than the pitting potential of the uncoated substrate ( $0.3 V_{SCE}$ ), the corrosion of the substrate at the coating–substrate interface is serious. This result suggests that the pitting potential of the substrate at the coating–substrate interface is lower than that of the uncoated substrate, which demonstrates that the sharp increase of current density for the unsealed coating as the potential exceeds  $0 V_{SCE}$  is due to the pitting of the substrate during the potentiodynamic polarization test (Fig. 4). Considering the corrosive environment, the lower pitting potential of the substrate at the coating–substrate interface is attributed to the crevice corrosion caused by through-microcracks. The narrow and deep through-microcracks in the coating behave similarly to confined spaces, which can obstruct the diffusion of oxygen and ions. This behaviour can be reflected by the existence of Warburg impedance in the EIS plots of the unsealed coating as shown in Fig. 6. When immersed in neutral solution, the corrosion of the metal is an electrochemical reaction. The anodic process is the dissolution of metal, while the cathodic reaction is the reduction of oxygen. As the corrosion proceeds, the oxygen inside the through-microcracks is exhausted and cannot be supplemented due to occlusion effect. Consequently, the cathodic reaction mainly occurs on the coating surface outside the microcrack, whereas the anodic reactions mainly occur inside the through-microcracks [35]. Thus, the metal dissolution current density within through-microcracks becomes high, which makes the  $Cl^-$  anions migrate into through-microcracks by electromigration. In addition, the hydrolysis of the dissolved metal cations leads to the acidification of the solution within the through-microcracks, especially at the bottom of the through-microcracks due to the more serious occlusion effect [35]. Both the increase of the concentration of chloride ions and the decline of pH value can decrease the pitting potential of stainless steel, while the pitting potential of amorphous coating is unaffected [13,25,36]. Therefore, the pitting corrosion of the substrate at the coating–substrate interface occurs at a lower potential than the pitting potential of the uncoated substrate. As shown in Fig. 4, the anodic current density of the unsealed coating increases sharply as the potential exceeds  $1 V_{SCE}$ , which results from the pitting corrosion of amorphous coating. It is noted that the pitting potential of the unsealed coating is a little higher than that of the sealed coating, which is ascribed to the cathodic protection caused by the pitting corrosion of the substrate. Because the

pitting potential of amorphous coating is much higher than that of the substrate and is not affected by the concentration of chloride ions and the pH value of solution, so the substrate dissolves rapidly while the amorphous coating is passivated for the unsealed coating at the potential range from 0  $V_{SCE}$  to 1  $V_{SCE}$  during the potentiodynamic polarization test. Thus, the amorphous coating acts as the cathode and its cathodic current density is larger than the anodic current density, which enhances the stability of passive film on coating surface.

On the basis of the previous results and analysis, the corrosion process of the unsealed coating during potentiostatic polarization test can be clarified and described. The NaCl solution can penetrate into the through-microcracks and reach the substrate, which leads to the crevice corrosion of the exposed substrate beneath the through-microcracks. Moreover, the relatively high porosity near the coating–substrate interface promotes the diffusion of corrosive solution along the coating–substrate interface [23], which results in the corrosion of the substrate at the coating–substrate interface. By contrast, the corrosion of the amorphous coating is slight because of passivation. As a result, a gap between the coating and the substrate forms. Furthermore, the gap also behaves like the confined space, which further facilitates the crevice corrosion of the substrate. This corrosion process causes the rapid increase of the current density at the initial stage of the potentiostatic polarization test as shown in Fig. 8. The corrosion products generate as the corrosion of the substrate. As the resultant of the corrosion reaction, the corrosion products, which are mainly the oxides or hydroxides of metal, have higher mass and lower density than the reactive metal. Therefore, the volume of corrosion products is much larger than that of the reactive metal, which makes corrosion products fill in the gap between the coating and substrate as well as the through-microcracks as shown in Figs. 9b and c respectively. When the gap and the microcracks are completely filled, the excess corrosion products will flow out of the microcracks and pile up on the coating surface as shown in Fig. 9d. The formation and accumulation of the corrosion products can plug the ion mass transfer channels between the substrate and the outer corrosive solution, which prevents the increase of corrosion rate. Therefore, the current density stops rising and fluctuates within a small range at the later stage of the potentiostatic polarization test as shown in Fig. 8.

Fig. 10 shows another typical cross-section morphology of the unsealed coating after potentiostatic polarization test. The red straight line marks the coating surface on the left of the microcrack and the blue straight line marks the coating surface on the right. It is worth noting that there is a small angle between the coating surfaces on both sides of the microcrack. The emergence of the angle may result from the accumulation of corrosion products in the gap between the coating and the substrate beneath the microcrack. The serious corrosion of the substrate produces much corrosion products, which fully fill in the gap between the coating and substrate along with the microcracks, and the excess corrosion products flow out of the microcracks. However, the narrow microcrack restricts the outflow of the corrosion products. As a result, the formation of the corrosion products is faster than the outflow, which leads to the accumulation of corrosion products in the gap between the coating and substrate beneath the microcrack. The accumulated corrosion products in the gap can produce a force that separates the coating from the substrate and enlarges the gap between the coating and substrate beneath the microcrack. Consequently, a small angle appears between the coating surfaces on both sides of the microcrack.

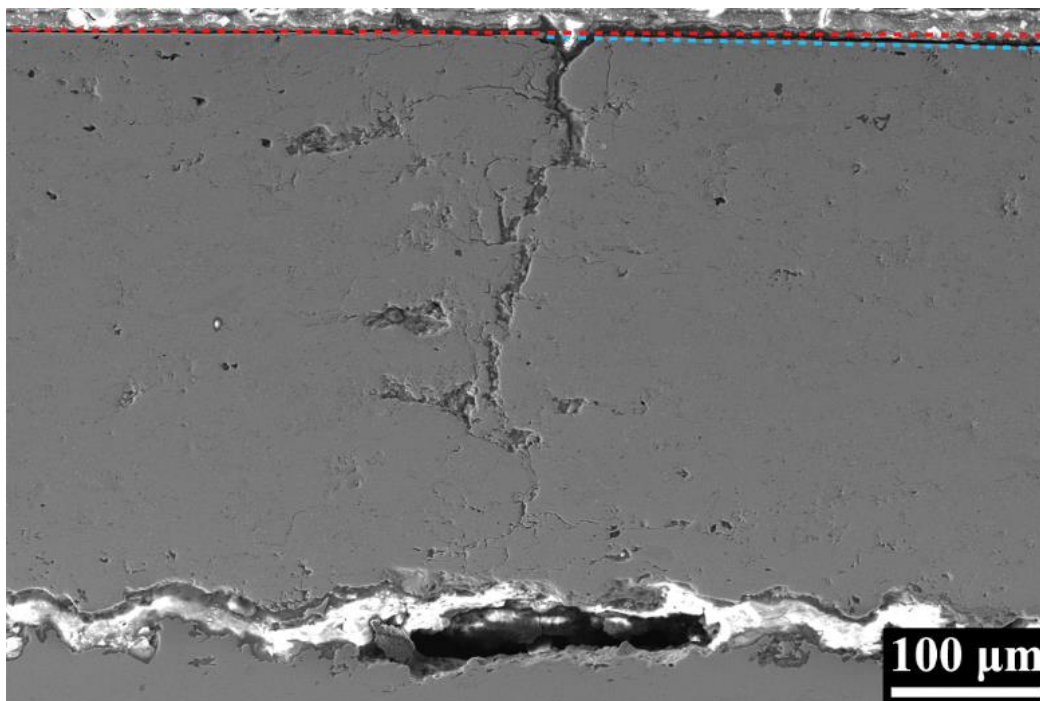


**Figure 10.** Cross-sectional morphology of unsealed coating after potentiostatic polarization test in 3.5 wt.% NaCl solution.

#### 4. CONCLUSION

The role of microcracks in the corrosion behaviour of the coated 304 stainless steel was investigated and the conclusions are summed up as follows:

(1) The through-microcracks in Fe-based amorphous coating can be penetrated by corrosive solution, which leads to the direct corrosion of the substrate. Besides, the pitting potential of the coated substrate decreases due to the crevice corrosion caused by through-microcracks.

(2) The through-microcracks can be sealed after sealing treatment, which prevents the penetration of corrosive solution.

(3) Corrosion products have an important effect on the corrosion of unsealed coating. On the one hand, the corrosion products filled in the defects of coating prevent the increase of corrosion rate. On the other hand, the accumulated corrosion products in the gap between the coating and substrate facilitate the separation of the coating and substrate.

#### ACKNOWLEDGEMENTS

This work was supported by the National Natural Science Foundation of China (grant numbers 51601129, 51401051 and 51601130) and Shanghai Natural Science Foundation (grant number 13ZR1462400).

#### References

1. C. Suryanarayana and A. Inoue, *Int. Mater. Rev.*, 58 (2013) 131.
2. C. A. C. Souza, D. V. Ribeiro and C. S. Kiminami, *J. Non-Cryst. Solids*, 442 (2016) 56.
3. H. B. Wang, L. X. Ma, L. Li and B. Zhang, *J. Alloys Compd.*, 629 (2015) 1.

4. S. F. Guo, L. Liu, N. Li and Y. Li, *Scr. Mater.*, 62 (2010) 329.
5. Z. F. Zhang, F. F. Wu, W. Gao, J. Tan, Z. G. Wang, M. Stoica, J. Das, J. Eckert, B. L. Shen and A. Inoue, *Appl. Phys. Lett.*, 89 (2006) 251917.
6. P. A. Hess, S. J. Poon, G. J. Shiflet and R. H. Dauskardt, *J. Mater. Res.*, 20 (2005) 783.
7. W. M. Guo, Y. P. Wu, J. F. Zhang, S. Hong, G. Y. Li, G. B. Ying, J. Guo and Y. J. Qin, *J. Therm. Spray Technol.*, 23 (2014) 1157.
8. Y. Y. Zhou, G. Z. Ma, H. D. Wang, G. L. Li, S. Y. Chen and B. G. Fu, *J. Therm. Spray Technol.*, 26 (2017) 1257.
9. H. R. Ma, J. W. Li, J. Jiao, C. T. Chang, G. Wang, J. Shen, X. M. Wang and R. W. Li, *Mater. Sci. Technol.*, 33 (2017) 65.
10. Y. Wang, K. Y. Li, F. Scenini, J. Jiao, S. J. Qu, Q. Luo and J. Shen, *Surf. Coat. Technol.*, 302 (2016) 27.
11. R. Q. Guo, C. Zhang, Q. Chen, Y. Yang, N. Li and L. Liu, *Corros. Sci.*, 53 (2011) 2351.
12. S. J. Choi, H. S. Lee, J. W. Jang and S. Yi, *Met. Mater. Int.*, 20 (2014) 1053.
13. Y. Wang, Z. Z. Xing, Q. Luo, A. Rahman, J. Jiao, S. J. Qu, Y. G. Zheng and J. Shen, *Corros. Sci.*, 98 (2015) 339.
14. Y. Wang, S. L. Jiang, Y. G. Zheng, W. Ke, W. H. Sun and J. Q. Wang, *Surf. Coat. Technol.*, 206 (2011) 1307.
15. M. M. Liu, H. X. Hu and Y. G. Zheng, *Surf. Coat. Technol.*, 309 (2017) 579.
16. L. Liu and C. Zhang, *Thin Solid Films*, 561 (2014) 70.
17. H. S. Ni, X. H. Liu, X. C. Chang, W. L. Hou, W. Liu and J. Q. Wang, *J. Alloys Compd.*, 467 (2009) 163.
18. Y. Wang, Y. G. Zheng, W. Ke, W. H. Sun, W. L. Hou, X. C. Chang and J. Q. Wang, *Corros. Sci.*, 53 (2011) 3177.
19. R. Q. Guo, C. Zhang, Y. Yang, Y. Peng and L. Liu, *Intermetallics*, 30 (2012) 94.
20. P. Xu, C. Zhang, W. Wang and L. Liu, *Electrochim. Acta*, 206 (2016) 61.
21. C. Zhang, R. Q. Guo, Y. Yang, Y. Wu and L. Liu, *Electrochim. Acta*, 56 (2011) 6380.
22. C. Zhang, K. C. Chan, Y. Wu and L. Liu, *Acta Mater.*, 60 (2012) 4152.
23. S. D. Zhang, W. L. Zhang, S. G. Wang, X. J. Gu and J. Q. Wang, *Corros. Sci.*, 93 (2015) 211.
24. S. D. Zhang, J. Wu, W. B. Qi and J. Q. Wang, *Corros. Sci.*, 110 (2016) 57.
25. J. Jiao, Q. Luo, X. S. Wei, Y. Wang and J. Shen, *J. Alloys Compd.*, 714 (2017) 356.
26. H. Zhang, Y. T. Xie, L. P. Huang, S. S. Huang, X. B. Zheng and G. Chen, *Surf. Coat. Technol.*, 258 (2014) 495.
27. Y. P. Wu, P. H. Lin, G. Z. Xie, J. H. Hu and M. Cao, *Mater. Sci. Eng., A*, 430 (2006) 34.
28. K. Chokethawai, D. G. McCartney and P. H. Shipway, *J. Alloys Compd.*, 480 (2009) 351.
29. A. A. Morquecho, A. C. Castilla, C. L. Porras, J. A. A. Martinez, G. V. Gutiérrez, K. J. M. Bello, and L. L. López, *Adv. Mater. Sci. Eng.*, 2014 (2014) 1.
30. F. Shao, K. Yang, H. Y. Zhao, C. G. Liu, L. Wang and S. Y. Tao, *Surf. Coat. Technol.*, 276 (2015) 8.
31. C. Liu, Q. Bi, A. Leyland and A. Matthews, *Corros. Sci.*, 45 (2003) 1243.
32. C. Liu, Q. Bi and A. Matthews, *Corros. Sci.*, 43 (2001) 1953.
33. X. H. Zhao, Y. Zuo, J. M. Zhao, J. P. Xiong and Y. M. Tang, *Surf. Coat. Technol.*, 200 (2006) 6846.
34. C. Zhong, X. Tang and Y. F. Cheng, *Electrochim. Acta*, 53 (2008) 4740.
35. Q. Hu, G. A. Zhang, Y. B. Qiu and X. P. Guo, *Corros. Sci.*, 53 (2011) 4065.
36. Y. Wang, Y. G. Zheng, W. Ke, W. H. Sun and J. Q. Wang, *Mater. Corros.*, 63 (2012) 685.